Joule

A decade of insights: Delving into calendar aging trends and implications

Graphical abstract

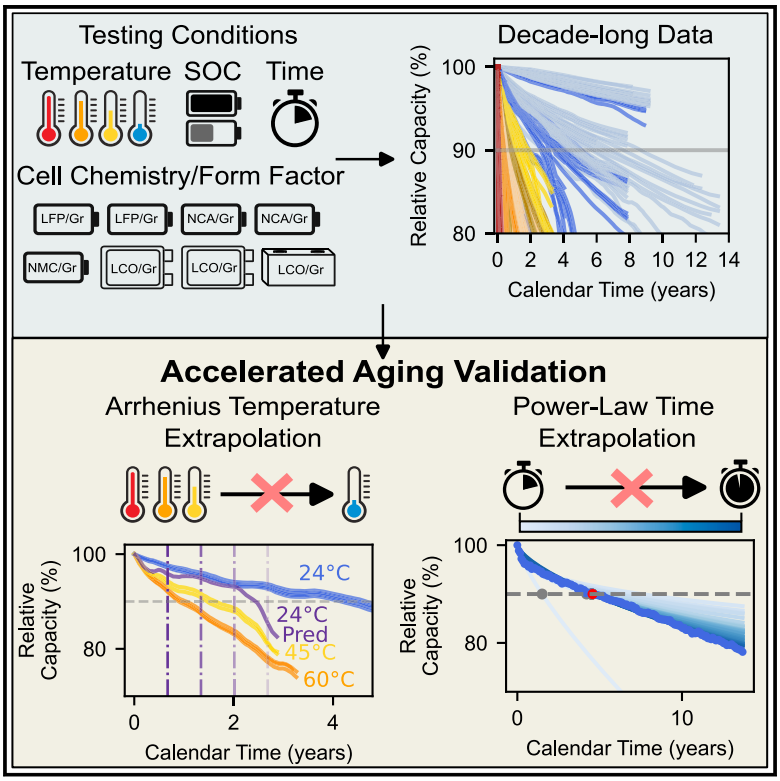

Highlights

- We share a dataset of commercial cells that endured calendar aging over 13 years
- We test the Arrhenius law for explaining temperature dependence on calendar aging
- We demonstrate the range of power-law exponents describing storage-time dependence
- We present the error in capacity fade predictions using these dependencies

Authors

Vivek N. Lam, Xiaofan Cui, Florian Stroebl, Maitri Uppaluri, Simona Onori, William C. Chueh

Correspondence

sonori@stanford.edu (S.O.), wchueh@stanford.edu (W.C.C.)

In brief

We share a long-term dataset comprising eight commercial cells from five manufacturers, calendar aged over extended periods. We assess common principles used to model calendar aging, validating them over long timescales, with a focus on the Arrhenius law for temperature dependence and the power law for storage-time dependence. We observe that at long storage times, capacity fade predictions deviate from these principles and emphasize the need for more sophisticated models to accurately represent long-term calendar aging.

Lam et al., 2025, Joule 9, 101796
January 15, 2025
https://doi.org/10.1016/j.joule.2024.11.013

CellPress

Joule

CellPress
OPEN ACCESS

Article

A decade of insights: Delving into calendar aging trends and implications

Vivek N. Lam,[1,2,4] Xiaofan Cui,[3,4] Florian Stroebl,[3,4] Maitri Uppaluri,[2,3] Simona Onori,[2,3,*] and William C. Chueh[1,2,3,5,*]
[1]Department of Materials Science and Engineering, Stanford University, Stanford, CA, USA
[2]Applied Energy Division, SLAC National Accelerator Laboratory, Menlo Park, CA, USA
[3]Department of Energy Science and Engineering, Stanford University, Stanford, CA, USA
[4]These authors contributed equally
[5]Lead contact
*Correspondence: sonori@stanford.edu (S.O.), wchueh@stanford.edu (W.C.C.)
https://doi.org/10.1016/j.joule.2024.11.013

CONTEXT & SCALE Calendar aging (capacity and power loss that occurs when the battery is at rest with no current) is a critical aspect of lithium-ion battery degradation, especially with the growing demand for electric transportation. The rate of calendar degradation depends on factors such as temperature and state of charge (SOC), with trends varying across cell types and chemistries.

This paper presents the capacity fade and resistance growth of various cells that underwent long-term calendar aging across a variety of storage temperatures and SOCs. The data reveal that commonly accepted laws for capacity fade do not apply across all cell types and operating conditions and that significant cell-to-cell variability in degradation exists even for the same operating conditions and cell type. These challenges must be accounted for when simulating or predicting cell aging for accelerated aging studies, real-time remaining useful-life prediction, or other applications.

SUMMARY

Lithium-ion batteries remain at rest for extended periods and experience calendar aging. Although lithium-ion batteries are expected to perform for over 10 years at room temperature, long-term calendar aging data are seldom reported over such timescales. We present a dataset from 232 commercial cells across eight cell types and five manufacturers that underwent calendar aging across various temperatures and states of charge (SOCs) for up to 13 years. We analyze calendar aging across these conditions by tracking capacity loss and resistance growth as the cells degrade. This dataset is used to validate simple models, primarily the Arrhenius law and the power law, which explain the temperature and storage time on calendar aging. Certain applications of Arrhenius and power law fail to describe the dependence of capacity loss on temperature and resistance growth on storage time. Through this dataset, we demonstrate the complexity of calendar aging and the challenges in reducing trends into phenomenological models.

INTRODUCTION

Lithium-ion batteries are crucial for a wide range of applications, including powering portable electronics, electrifying transportation, and decarbonizing the electricity grid.[1–3] In many instances, however, lithium-ion batteries only spend a small portion of their lifetime in operation, with the majority of their life spent under no applied load.[4] For example, electric vehicles spend about 90% of their time parked.[5,6] When lithium-ion batteries are under these conditions, they experience degradation due to calendar aging, where they lose capacity and become more resistive due to parasitic reactions.[7,8] Understanding calendar aging is critical to improve battery utilization in real-world scenarios and to prolong battery lifetime.

One of the greatest challenges in understanding calendar aging is that appreciable degradation at room temperature takes many years to collect. To address this challenge, calendar aging data are typically either collected at higher temperatures or at lower temperatures for a limited duration (see Figures S1 and S2 for a summary of calendar aging data from the literature collected at various temperatures and end-of-testing [EOT] conditions). These data are then used to develop accelerated aging models that extrapolate high-temperature data to low-temperature scenarios, short-term to long-term calendar aging, or data from one chemistry to batteries of similar chemistry.[9–11] In all of these cases, low-temperature validation data that span realistic operating timelines are necessary to validate the modeling efforts. The accuracy of these models relies on precise

predictions and modeling of the temperature and time dependencies. Most models focus on capturing the solid-electrolyte interphase (SEI) layer growth on the graphite anode because this has been widely accepted as the primary mechanism that contributes to calendar aging in lithium-ion batteries.[12–15] The baseline time-dependence model for the SEI layer growth is rooted in standard chemical kinetics, namely, the semi-infinite diffusion-limited growth of layers, resulting in a $t^{0.5}$ dependence on time.[16] Meanwhile, the temperature dependence of calendar aging is prevailingly described with Arrhenius-type expressions.[17–19] Together, the Arrhenius temperature dependence and the $t^{0.5}$ time dependence form the baseline of standard models used for calendar aging prediction and extrapolation.

Several calendar aging studies on commercial lithium-ion batteries with graphite anodes and various cathode chemistries have been conducted to establish the validity of conventional models, as summarized in Table S3. Keil et al. revealed that the capacity loss from calendar aging depends strongly on the graphite anode potential, the driving force for SEI layer growth, and identified that, overall, a self-passivating $t^{0.5}$ time dependence is observed across three different cell types.[7] Bischof et al. identified that calendar aging in nickel-manganese-cobalt (NMC) cells follows $t^{0.5}$ and Arrhenius temperature behavior for graphite-based anodes with varying fractions of silicon.[20] Similarly, others have observed that cells with lithium-iron-phosphate (LFP) cathodes follow the $t^{0.5}$ behavior of capacity fade across different temperatures and states of charge (SOC).[21–23] However, because several theories exist to explain the mechanisms of the SEI layer growth, deviations from simple diffusion-limited growth models are expected. Research has shown that SEI growth deviates from the $t^{0.5}$ time dependence, and instead, general power-law models (t^b) should be used to better capture the time dependence.[24] Others have found that commercial cells with NMC and nickel-cobalt-aluminum (NCA) cathodes deviate from the $t^{0.5}$ time dependence of capacity fade but adhere to the Arrhenius law for temperature dependence.[19,25,26] Departures from both time and temperature ideality can also result from other non-SEI degradation mechanisms, such as cathode electrolyte interface (CEI) growth, transition metal dissolution, and copper current collector dissolution, as well as different temperature-dependent dominant degradation modes.[27–32] Additionally, different electrode manufacturing, electrolyte formulation, and cell form factors can contribute to differences among similar chemistries.[33] To account for these discrepancies, models that describe and predict the time dependence of calendar aging have been evolving, moving from diffusion-limited square root ($t^{0.5}$) law models to more sophisticated machine learning models.[8,11,16,24,34,35] However, these models still need long-time calendar aging validation because errors in model parameter identification can lead to amplified errors when extrapolating to distant times.[33] Additionally, combining data across individual chemistries and cells from the literature is challenging because aging experiments were conducted under unique characterization protocols and operating conditions.[9,36,37]

Calendar aging studies span from a few months to 5 years; however, realistic ambient temperature calendar lifetimes are in the order of 10 years. Table S3 summarizes the EOT conditions reported in different studies across the literature. The literature demonstrates that the calendar aging trends shift with time.[34,38–40] For instance, a recent study captured higher temperature calendar-aging data for 5 years on Ni-rich 18650 cells with silicon/graphite anodes and found that passive anode overhang had a transitory effect on calendar aging for a year of storage, after which a linear aging trend emerged.[39] Krupp et al. showed that the value of the exponent in the power law (b in t^b) changes when longer times of calendar aging are considered, going from an exponent close to 0.5 within 220 days to a drastically higher exponent (from 0.581 to 0.781) by 420 days, similar to "knees" observed in cycling aging.[38] Additionally, Lewerenz et al. observed deviations from the Arrhenius dependence on capacity loss only at long timescales.[41] These studies indicate that models validated with short-term aging data may not accurately represent the true degradation effects over long timescales.

In this work, we present long-term calendar aging data consisting of 232 cells across eight different cell types, four chemistries, and five manufacturers, collected for a period for up to 13 years, as shown in Table 1. The dataset used in this work is compared with data in the literature, summarized in Figures S1 and S2. Using these data, we systematically evaluate the validity of simple models and assumptions. We first examine the calendar aging data between 25°C and 60°C to assess the Arrhenius temperature dependence. Under certain assumptions, we observe significant deviation from the expected Arrhenius trends, which can result in inaccurate estimates of room temperature degradation trends by several years. This temperature dependence varies significantly even among seemingly similar chemistry cells from the same manufacturer. Next, by analyzing the time dependence of degradation, we observe deviation from the ideal diffusion-limited growth $t^{0.5}$ toward less self-passivating values, along with a significant spread in ambient temperature degradation trends across chemistries. Furthermore, capacity and power fade exhibit distinct trends that are not well correlated. Finally, we show that cell-to-cell variability can account for a significant portion of degradation, highlighting the importance of understanding individual cell trajectories alongside population trends. These observations underscore the necessity to revisit calendar aging mechanisms and predictions concerning accelerated aging, early forecasting, and transfer learning studies.

RESULTS

Calendar aging data analysis

Calendar aging data were collected from 232 cells over 13 years, for eight distinct cell types from five manufacturers (Table 1). These batteries were stored at four temperatures (24°C, 45°C, 60°C, or 85°C) and two SOC values (50% and 100%, see methods for SOC definition). For each storage condition, at least three replicates were tested, allowing for an analysis of variability over the cells' lifetimes. To probe the battery capacity and resistance, a diagnostic cycle consisting of three C/5 cycles and three high-rate cycles (the high-rate C rate is variable per chemistry, see Table S2 for values) is performed at regular intervals of time during calendar aging (see methods).

In this work, we track normalized degradation for all cells, expressed as relative capacity ($Q_{rel}(t)[\%] = \frac{Q(t)}{Q(0)} \times 100\%$) and resistance ($R_{rel}(t)[\%] = \frac{R(t)}{R(0)} \times 100\%$) metrics (see methods for

Table 1. Cell chemistry summary

Manufacturer	Cell type	Form factor	Chemistry	Temperatures (°C)	SOC (%)	Total cells	Aging years
K2 Energy	LFP18650E	18650	LFP/Gr	24, 45, 60, 85	50, 100	40	7.8
K2 Energy	LFP18650P	18650	LFP/Gr	24, 45, 60, 85	50, 100	40	7.8
Panasonic	NCR18650B	18650	NCA/Gr	24, 45, 60, 85	50, 100	28	7.8
Panasonic	NCR18650GA	18650	NCA/Gr	24, 60, 85	50, 100	36	5.9
Sony-Murata	US18650VTC6	18650	NMC/Gr	24, 60, 85	100	18	5.3
Tenergy	302030	pouch	LCO/Gr	24, 60, 85	50, 100	32	9.1
Ultralife	502030	pouch	LCO/Gr	24	50, 100	20	13.7
Ultralife	UBP001	prismatic	LCO/Gr	24, 60, 85	100	18	1.0

Table summarizing the information of each of the cell types in this dataset. Aging years is the maximum time that a battery has been tested for. Cathode abbreviations used here are LFP ($LiFePO_4$), NCA ($Li(Ni, Co, Al)O_2$), NMC ($Li(Ni, Mn, Co)O_2$), and LCO ($LiCoO_2$). For further details on the cell capacities and testing, see Table S2.

calculation details). For each cell, relative capacity $Q_{rel}(t)$ (Figures 1A and 1B) and relative resistance $R_{rel}(t)$ (Figures 1C and 1D) are plotted as a function of calendar time. To better visualize the underlying trend, the data plotted in Figure 1 are smoothed (see methods for smoothing/filtering details). Although several cells have data continuing to deeper degradation (Figures S12–S15), the data are plotted only up to 80% relative capacity to emphasize the normal operational regime of batteries. To include a significant portion of the 24°C data, 90% relative capacity (indicated by a horizontal gray line) is defined as the end-of-life (EOL) condition in this paper. The variation, duration, and non-linearities observed in the degradation trends underscore the richness of the calendar aging information captured in the dataset.

Assessing Arrhenius rate dependence

The Arrhenius equation is widely used in the literature for modeling temperature dependence.[19,22,38,41] However, deviations from this dependency can lead to improper estimation of degradation at lower temperatures. At higher temperatures (>60°C), electrolyte decomposition and structural degradation of the cathode are expected.[42,43] These degradation mechanisms lead to deviations from the typical Arrhenius relationship for temperature dependence on capacity fade from calendar aging. To assess the validity of the Arrhenius equation applied to this dataset, we first examine an example cell type (Panasonic NCR18650B) stored across different temperatures (Figure 2A).

Although it is challenging to assess the validity of the Arrhenius rate dependence for arbitrary functional forms, we assess its applicability under certain assumptions. We start by defining relative capacity loss ($Q_{rel\_loss}(t)[\%] = 100\% - Q_{rel}(t)$). We then assume that the temperature, SOC, and time dependence of degradation are separable such that $Q_{rel\_loss}(T, SOC, t) = A(T) \times F(SOC) \times G(t)$, where *F(SOC)* is a non-linear function of SOC. Assuming an Arrhenius dependence of the temperature function ($A(T) \propto a_0 \exp\left(\frac{-E_a}{k_b T}\right)$, where E_a is the activation energy, and k_b is the Boltzmann constant) result in a linear relationship between $ln(Q_{rel\_loss}(t))$ and $ln(1/T)$ for arbitrary time functions ($G(t)$) at fixed times, regardless of SOC (see Equation S10, for further derivations and explanations of this approach in Section S1.2).[22,41] We use this relationship to generate an Arrhenius plot at four degradation time points (35, 70, 105, and 140 weeks), as shown in Figure 2B. These time points are indicated by vertical dashed lines in Figure 2A. If the Arrhenius equation holds under these assumptions, the traces should be linear with the same slope (activation energy) at all time points. Instead, we observe a significant deviation in the data (solid line) from the expected ideal behavior (dashed line) (in Figure 2B). Although the data seem to follow Arrhenius behavior at the middle time points, (70 and 105 weeks), significant deviations are observed at the beginning and end of the dataset (35 and 140 weeks) when examining the full lifetime (35 and 140 weeks). To highlight the deviation, we refit the Arrhenius equation at each time point using the 45°C and 60°C data and then extrapolate to 24°C to generate the Arrhenius-predicted degradation curve for 24°C. This prediction (shown in Figure 2A) estimates the calendar life at EOL to be 128 weeks. Experimentally, however, the observed calendar life is 231 weeks, representing a nearly 2-year discrepancy. The Arrhenius-predicted degradation curve for 24°C is also shown for other cell chemistries and testing conditions in Figures 2C–2E. Although the predicted trend aligns best with K2 Energy LFP18650P cells, significant deviations are observed under most conditions.

One could attribute this deviation to the breaking of the temperature and time separability assumption. Indeed, temperature-dependent time dependencies are observable in Figure 2A. In particular, any cells exhibiting knees, such as the NCA cells in Figures 2A and 2E, significantly violate the separability assumptions. Because testing the Arrhenius approximation for completely arbitrary functional forms is not feasible, we instead assume standard semi-empirical power laws as the functional form and parameterize individual battery degradation curves without assuming any dependence. Using this framework, we analyze the dependence of the coefficients directly. The power-law equations used for relative capacity and relative resistance growth are as follows:

$$Q_{rel}(t)[\%] = 100\% - a_Q t^{b_Q} \quad \text{(Equation 1)}$$

$$R_{rel}(t)[\%] = 100\% + a_R t^{b_R} \quad \text{(Equation 2)}$$

where the exponential parameter (b_Q or b_R, dimensionless units) captures the time-dependent behavior of degradation

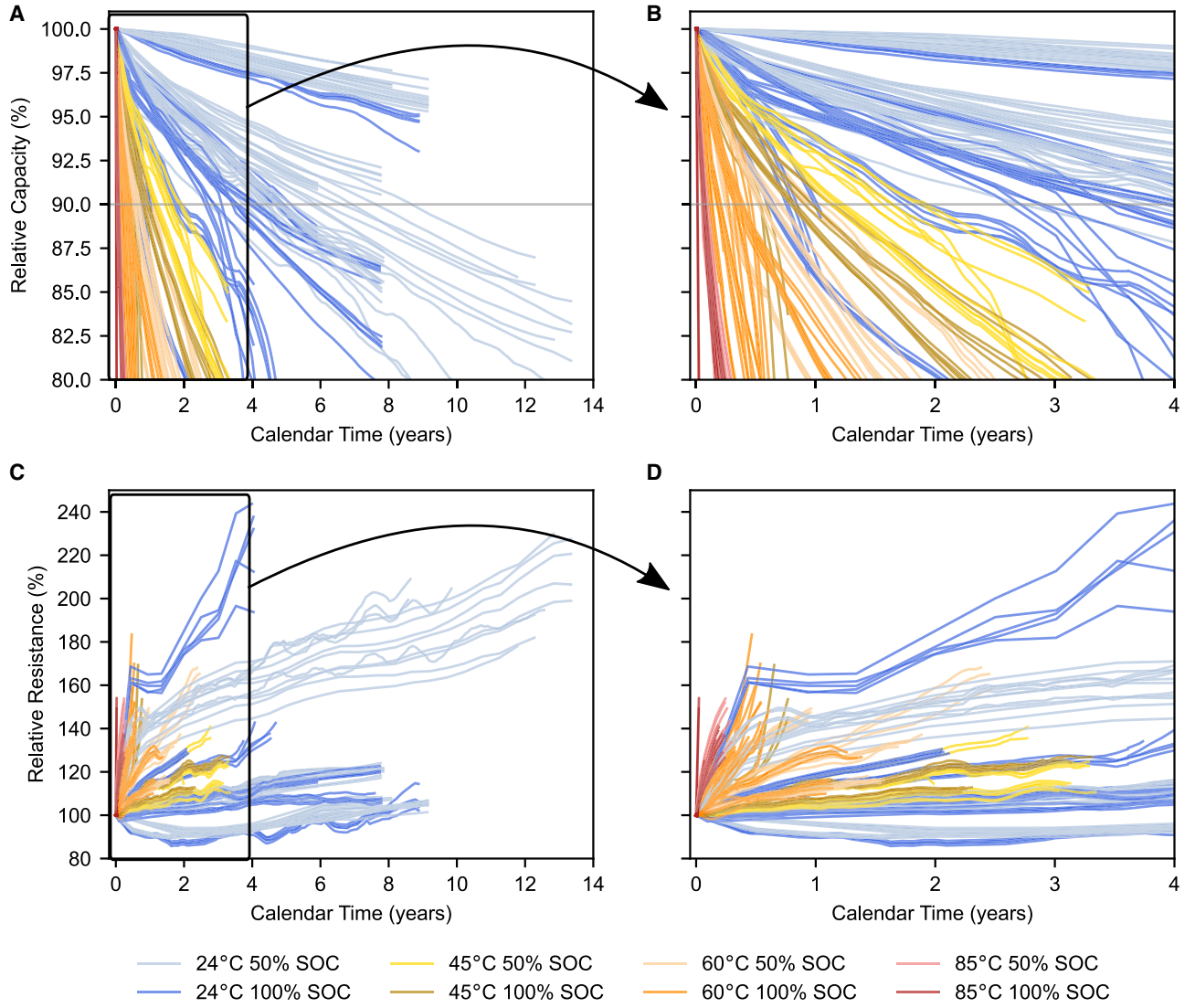

Figure 1. Overview of relative capacity and relative resistance calendar aging trends

(A) Relative C/5 discharge capacity (Q_{rel}) trends. A gray line is shown at the 90% capacity loss EOL condition.

(B) Zoom-in view of the black box highlighted in (A) to better visualize the higher temperature data.

(C) The trajectory of relative resistance (R_{rel}).

(D) Zoom-in view of the box in (C) to show the higher temperature trends. All trajectories shown here are smoothed (see methods). For individual unfiltered trajectories see Figures S12–S15).

and the pre-exponential parameter (a_Q or a_R, units of %/$weeks^b$) encodes the rate of degradation (see Section S1.1 for definitions in terms of capacity loss and resistance growth). We fit these equations to capacity and resistance data up to the 90% capacity EOL condition (see methods for fitting details). Although we do not expect this simple semi-empirical equation to fully capture the complexities of calendar aging degradation (see Figure S3 for time-dependent non-linearity of fitting), we use this framework to quantitatively evaluate trends of *a* and *b* parameters of capacity loss and resistance growth across temperature, SOC, and cell type. Because the accuracy of the results depends on the quality of fit, we report the mean absolute errors in Figure S9.

After fitting all the degradation curves, we revisit the Arrhenius dependence by applying it to the *a* parameters a_Q and a_R ($a \propto a_0 \exp\left(\frac{-E_a}{k_b T}\right)$). For cell types with three or more temperature data points, the fits are shown in an Arrhenius plot (Figure 3). Once again, we see that the data do not align with a straight line of constant activation energy (E_a) for either capacity or resistance for all cell types. Deviation from this linearity violates the Arrhenius assumption and likely indicates temperature-dependent activation energy, simultaneous degradation mechanisms, complex reaction pathways, and/or changing

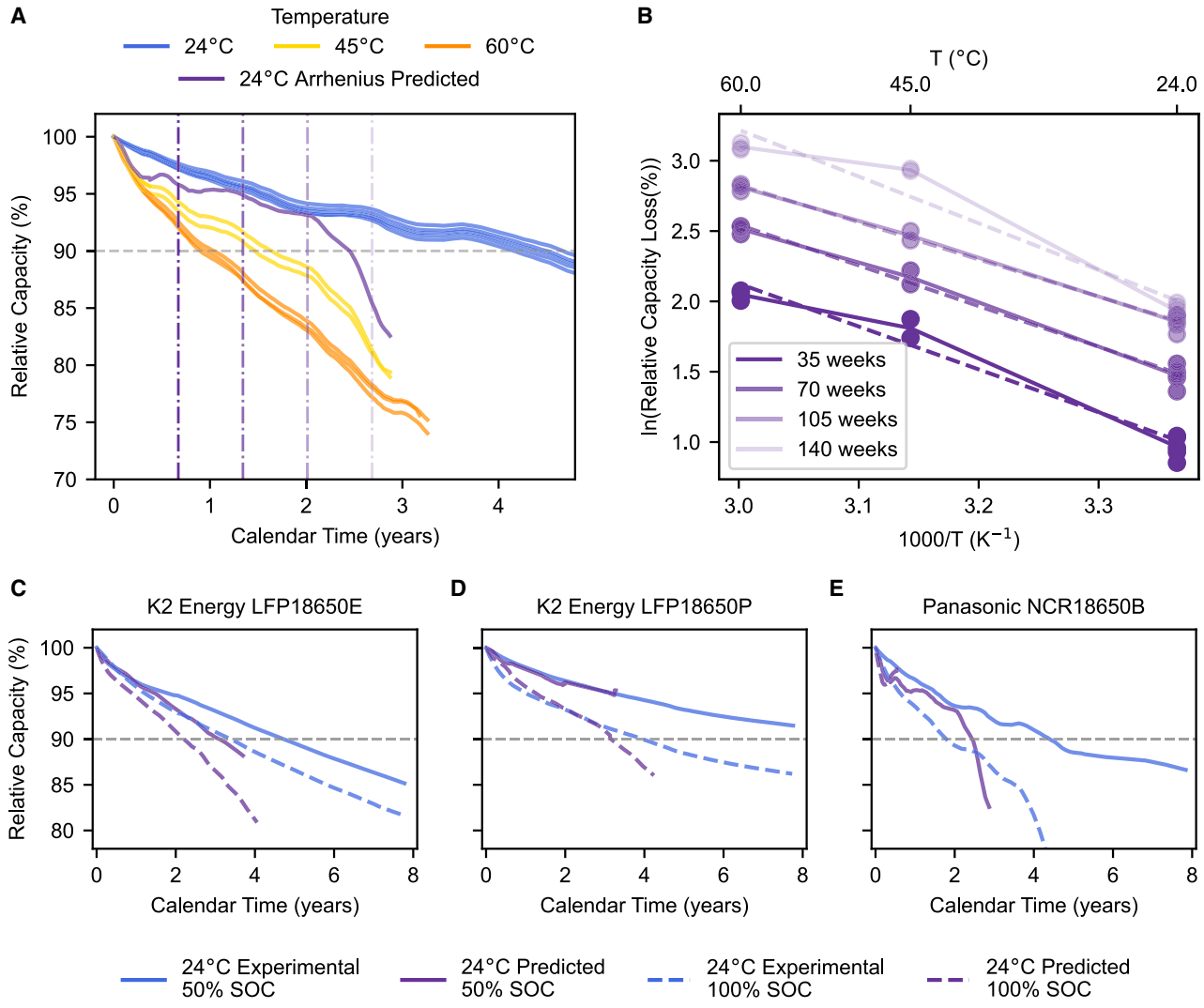

Figure 2. Temperature dependence of degradation

An example of temperature-dependent degradation is shown for Panasonic NCR18650B at 50% SOC.

(A) Relative capacity (Q_{rel}) vs. time curve with dashed lines showing the calendar times at which capacity is extracted across different temperatures and plotted in (B). The purple curve is the degradation trend extrapolated from 45°C and 60°C using the Arrhenius plot in (B). (B) Relative capacity loss (Q_{rel_loss}) points taken from the dashed lines in (A) are plotted on an Arrhenius plot.[41] The increasing transparency indicates increasing time. The dashed line shows the line of best fit representing ideal Arrhenius behavior, whereas the solid line connects the means (the means of the relative capacities losses from each cell at a given temperature). The discrepancy between these two lines demonstrates the deviation from the Arrhenius dependence on calendar aging. Fitting a line through the 45°C and 60°C points and extrapolating to 24°C at all time points gives the predicted 24°C degradation curve shown in (A). This degradation curve predicted from the Arrhenius law is additionally compared with the 24°C experimental data for (C) K2 Energy LFP18650E, (D) K2 Energy LFP18650P, and (E) Panasonic NCR18650B cells for both 50% and 100% SOC. To see plots including the higher temperature data, see Figure S4.

degradation modes. These results highlight the need for caution when applying the Arrhenius assumption to extrapolate lifetimes at different temperatures, particularly in use cases such as accelerated aging studies, where prediction of ambient temperature calendar aging is critical to save resources and time.

Capacity and resistance degradation dependence on operating conditions

Although we have shown that the Arrhenius approximation may not always hold, we still compute the average activation energies by fitting a line of best fit using the $\leq$60° C data shown for cell types with more than two tested temperatures in Figure 3 (data for all cell types, as well as fitting details, are shown in Figures S5–S7 and Section S1.3). This analysis allows us to compare the severity of the temperature influence across different cell chemistries (Figure 4). In general, the activation energy for capacity decreases with increasing SOC, whereas this trend is largely reversed for resistance. In general, the resistance growth has larger activation energies compared with capacity fade. Ultralife UBP001 cells seem to be the exception, with the

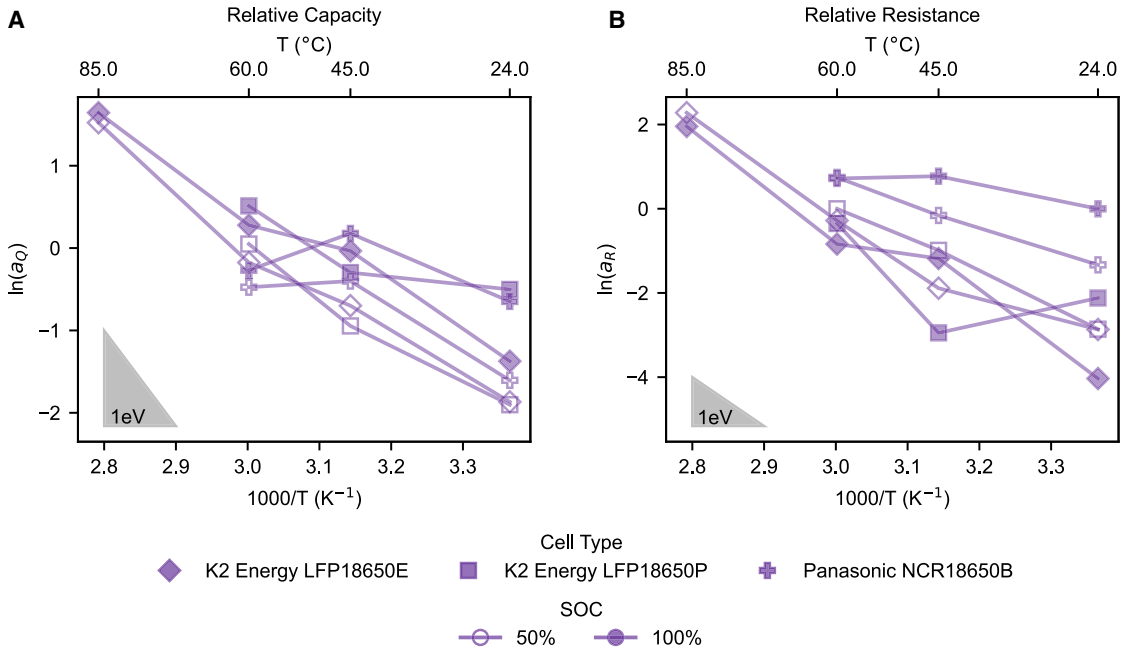

Figure 3. Arrhenius plot of semi-empirical modeling

The parameters (A) a_Q and (B) a_R are plotted on an Arrhenius plot. A slope is shown for an activation energy equal to 1 eV for reference. Only cell types with three or more temperatures tested are plotted here to showcase deviation from linear trends. For all cell types including those with only two temperatures, see Figure S5.

largest capacity calendar aging activation energy and one of the lowest resistance calendar aging activation energies. Interestingly, cells of similar chemistry from the same manufacturer can exhibit significantly different temperature dependencies. Although the K2 Energy LFP cells (LFP18650E vs. LFP18650P) have nearly identical relative-capacity temperature dependence at 50% SOC, at 100% SOC, and for relative resistance, they have vastly different temperature dependencies. Additionally, the Panasonic NCA cells (NCR18650B vs. NCR18650GA) have different temperature dependencies for all conditions. This observation underscores the challenges associated with transfer learning approaches, where data from similar cell chemistries may not reliably predict each other's behavior.

Next, we focus on the time dependence of degradation by analyzing the exponential parameter b for the relative capacity and the relative resistance across all testing conditions (Figure 5). The majority of the relative capacity time dependence across testing conditions and cell types show significant deviations from the semi-infinite, diffusion-limited growth $t^{0.5}$ dependence (Figure 5A).[24] Although most cell types do experience varying degrees of self-passivating capacity time dependence ($b_Q \leq 1$), some LCO ($LiCoO_2$) cells (namely, Tenergy 302030, and Ultralife UBP001) experience linear to super-linear capacity degradation. Notably, despite all cells having a graphite-based anode, there is no single b value that accurately describes degradation across testing conditions and temperatures. This is further illustrated in the histogram, where b_Q and b_R values at 24°C are highlighted in blue, showing a broad distribution across cell types (Figure 5). Additionally, within individual cell types, there is no evident temperature dependence of the b_Q and b_R values.

To further explore the relationship between resistance growth and capacity loss due to calendar aging, we directly compare the fitted parameters a_Q vs. a_R, and b_Q vs. b_R (Figure 6; Figure S10 analyzes the correlation on a per-cell-type basis). While the a_Q and a_R show a clear dependence on temperature and exhibit reasonable correlations, the b_Q and b_R, on the other hand, display no obvious temperature dependence and show weaker correlations. These results suggest that capacity and power loss trajectories in batteries are generally decoupled with each exhibiting different temperature dependencies. These differences can stem from non-linearities in SEI thickness vs. resistivity, cathode electrolyte interphase growth, and other phenomena.

Finally, we use the replicates in the dataset to assess the influence of cell-to-cell variability on the degradation trends of cells undergoing the same storage conditions. To quantify the extent of this cell-to-cell variability in the dataset, the coefficient of variation (CoV), defined as the standard deviation divided by the mean at a given time is plotted against the relative mean capacity loss (Figure 7). The CoV is interpolated at 1% increments of relative mean capacity loss reaching either EOL or EOT for capacity (Figures 7A–7D) and resistance (Figures 7E–7H). Some storage conditions exhibit several percent of variation within just the first 10% relative capacity loss, indicating a significant portion of the degradation. This variation takes several different shapes dictated by the individual underlying battery degradation trends. Examples of cells exhibiting growing variability are shown in Figures 7I and 7K, whereas those with shrinking variability are presented in Figures 7J and 7L.

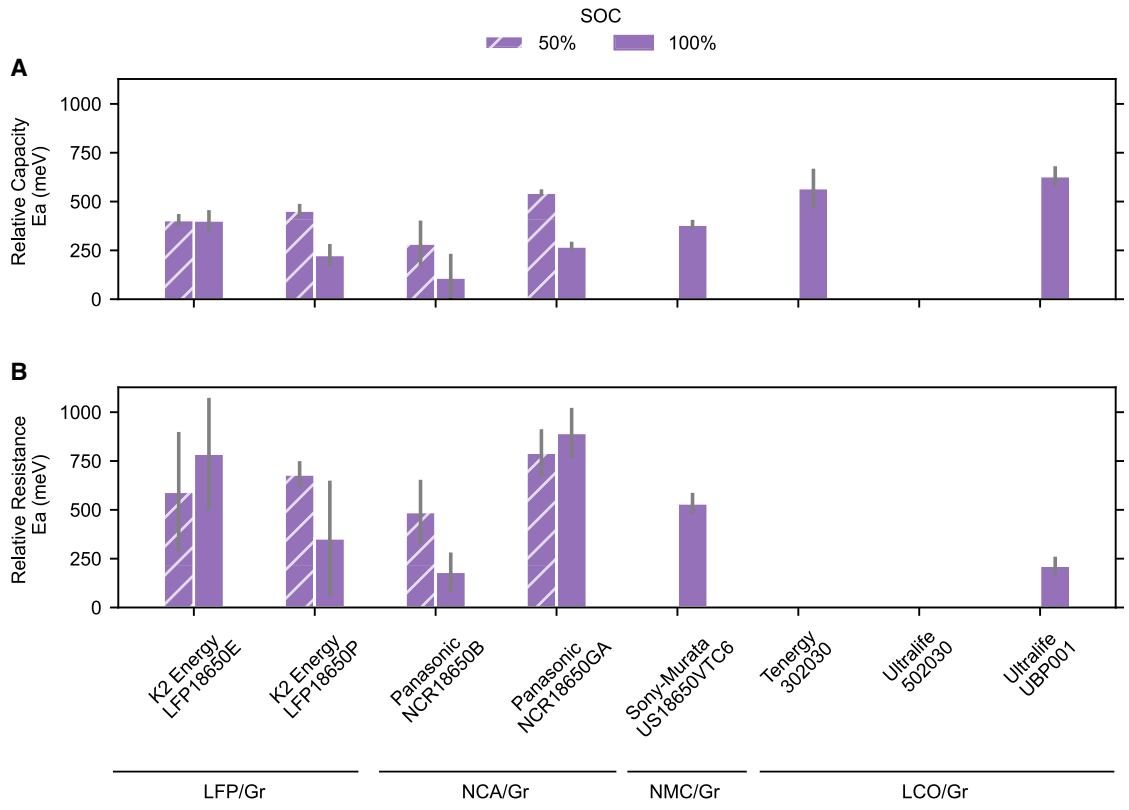

Figure 4. Activation energy dependence on chemistry and SOC

Bar plot of the activation energy in units of meV for (A) relative capacity and (B) relative resistance. These values are extracted from the slope on an Arrhenius plot using temperatures $\leq 60^{\circ}$C (see Figures 3 and S5–S7 and Section S1.3 for further details). The error bar plotted is the 90% confidence interval of the extracted slope. If data are only present for one temperature, the activation energy is not extracted. In the case of the Tenergy 302030 cells, the 24°C resistance growth is very flat, leading to an a_R close to 0 that could not properly be transformed into a log space and thus cannot be used.

From these plots it is evident that individual degradation trends can vary significantly from one another. Therefore, it is critical for calendar aging models to accurately capture the different battery trend lines resulting from cell-to-cell variability, otherwise the population behavior of batteries under given storage conditions can be misrepresented by significant percentages.[44]

Extrapolating calendar aging data is an effective way to significantly reduce the time required for data collection. To confidently perform this extrapolation, it is essential to understand the amount of data needed for an accurate forecast of the battery's EOL. To quantify this, we analyze the relative-capacity power-law fit using an increasing number of data points up to the EOL time, observing how the error changes over time (see methods for a full description). The power-law function well characterizes the trajectory, motivating our use of this simple functional form for testing early prediction. This methodology is illustrated with an example cell (C00214, K2 Energy LFP18650E, 24°C, 100% SOC) in Figures 8A and 8B. In general, using data closer to EOL leads to better estimations of the EOL, but the trajectory of the error is not monotonic. In Figure 8B, the power-law model initially underpredicts calendar life by over 2 years, then overpredicts by 4 years before converging on the correct EOL as more data are included.

The trajectory of the error is plotted for all 24°C cells in terms of both the absolute calendar time (Figure 8C) and the fraction of time until EOL (Figure 8D). Purple-shaded areas represent error boundaries predicting the EOL within ±2, 1, 0.5, and 0.25 years. To summarize these plots, the fraction of cells predicted within these four error boundaries are shown in Figures 8E and 8F. From this, we see that to predict 90% of all cells within ±0.5 years takes almost 5 years or 90% of the time until EOL. This amount of data is not conducive to reducing the data collection time of calendar aging studies and highlights the poor extrapolation capabilities of power-law models. Instead, advanced data-driven or electrochemical models are needed to properly utilize a smaller fraction of data to extrapolate cell performance to EOL and perform accelerated aging studies.

Developing accurate models that capture long-term calendar aging are crucial for predicting cell performance till EOL. This can take up to 15 years for electric vehicles (EVs).[45] However, as we demonstrated in this work, long-term calendar aging studies require significant time for experimentation and validation while ensuring versatility across different storage conditions and cell chemistries and accounting for the cell-to-cell variability. The deviation from expected trends observed with this dataset may be attributed to the accelerated lithium-ion loss or loss of active material. Various models can be used to simulate and predict

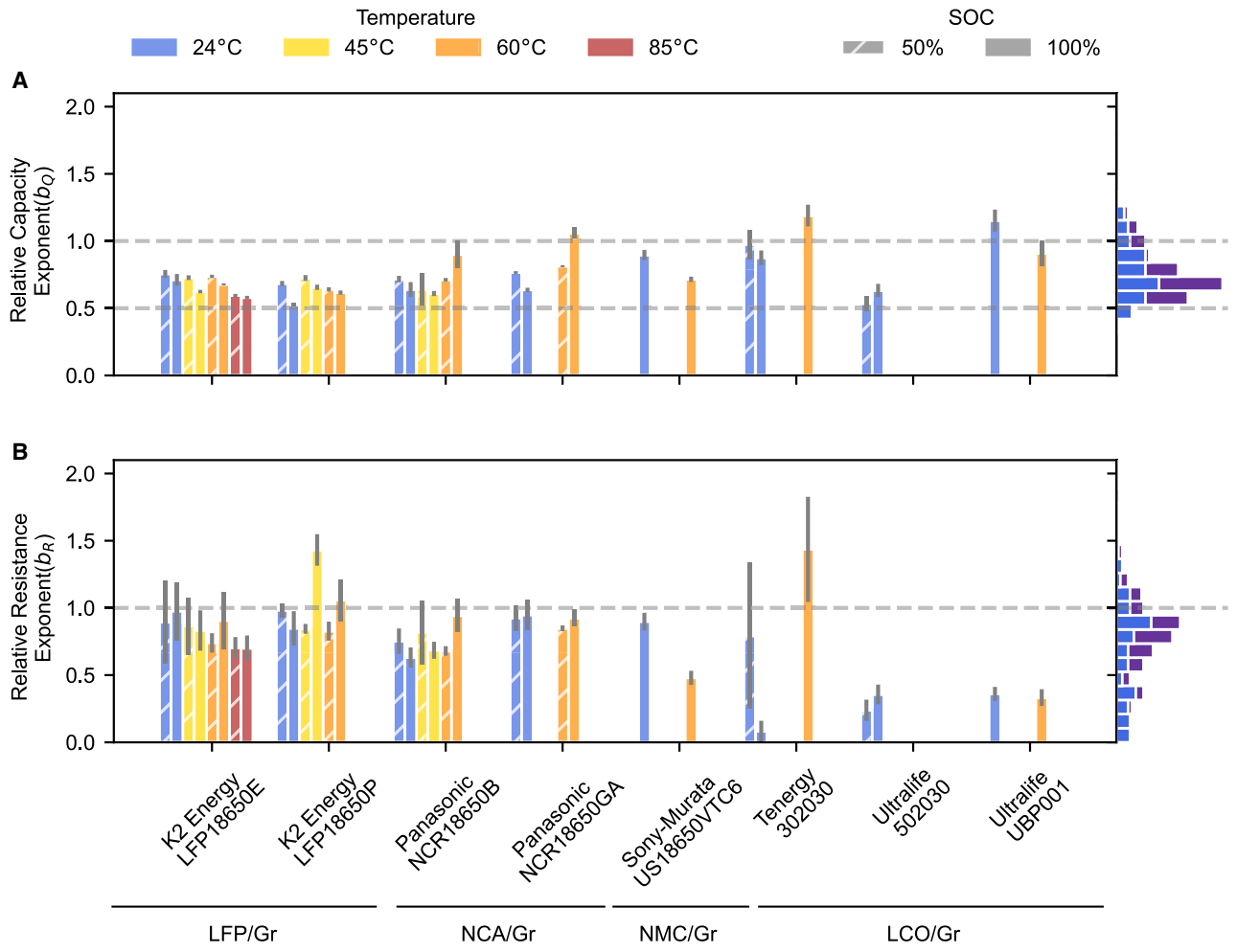

Figure 5. Exponential parameter dependence on aging conditions

Bar plots of the exponential parameter for (A) relative capacity and (B) relative resistance. A dashed line is shown at a parameter value of 0.5 for diffusion-limited growth for b_Q and 1 for the borderline of self-passivating vs. accelerating degradation for both b_Q and b_R. The error bar shown on the bar plot is the standard deviation of the b_Q and b_R values fit on replicates. Both bar plots have a histogram on the same x axis scale shown on the side for all b_Q or b_R values present in the dataset. The 24°C data contribution to the histogram is emphasized in blue. b_Q and b_R have a standard deviation value of 0.19 and 0.39, respectively. See Figure S8 for the pre-exponential parameter bar plot and Figure S9 for the mean absolute error of these fits.

calendar aging and can be validated using the dataset presented in this work. Electrochemical models are well suited for capturing individual degradation mechanisms to simulate and predict calendar aging from physics. The underlying mechanisms that cause calendar aging at specific SOCs and temperatures over long storage periods need to be understood to incorporate them into these models. Several efforts have been made to develop electrochemical models for calendar aging, focusing on the growth of the SEI layer as the dominant mechanism.[13,17,46,47] However, accurately capturing the degradation mechanisms models requires experimental validation during long-term calendar aging. Performing cell disassembly and employing advanced characterization techniques are useful for understanding degradation trends and to obtain model parameters that are influenced by calendar aging. Typical semi-empirical models for calendar aging employ the Arrhenius relationship and the power law for temperature and time dependence on capacity loss. There have been several efforts to enhance these models using advanced techniques such as symbolic regression, bi-level optimization, and data-driven approaches from machine learning tools. Symbolic regression utilizes algorithms to identify the optimal combination of functions that explain the dependence on temperature and SOC. For example, Gasper et al. employed symbolic regression to derive expressions for calendar aging, uncovering relationships that enhanced the accuracy of the aging models.[48] On the other hand, data-driven models, such as Gaussian process regression (GPR) and neural networks such as gated recurrent units (GRU) or long short-term memory (LSTM) for predicting the remaining useful life (RUL) or the capacity fade trajectories are gaining traction for calendar aging predictions.[10,40] Finally, stochastic models can be used over deterministic aging models to address cell-to-cell variability observed in this dataset, and several efforts have been made in literature to use stochastic models for predicting cycling

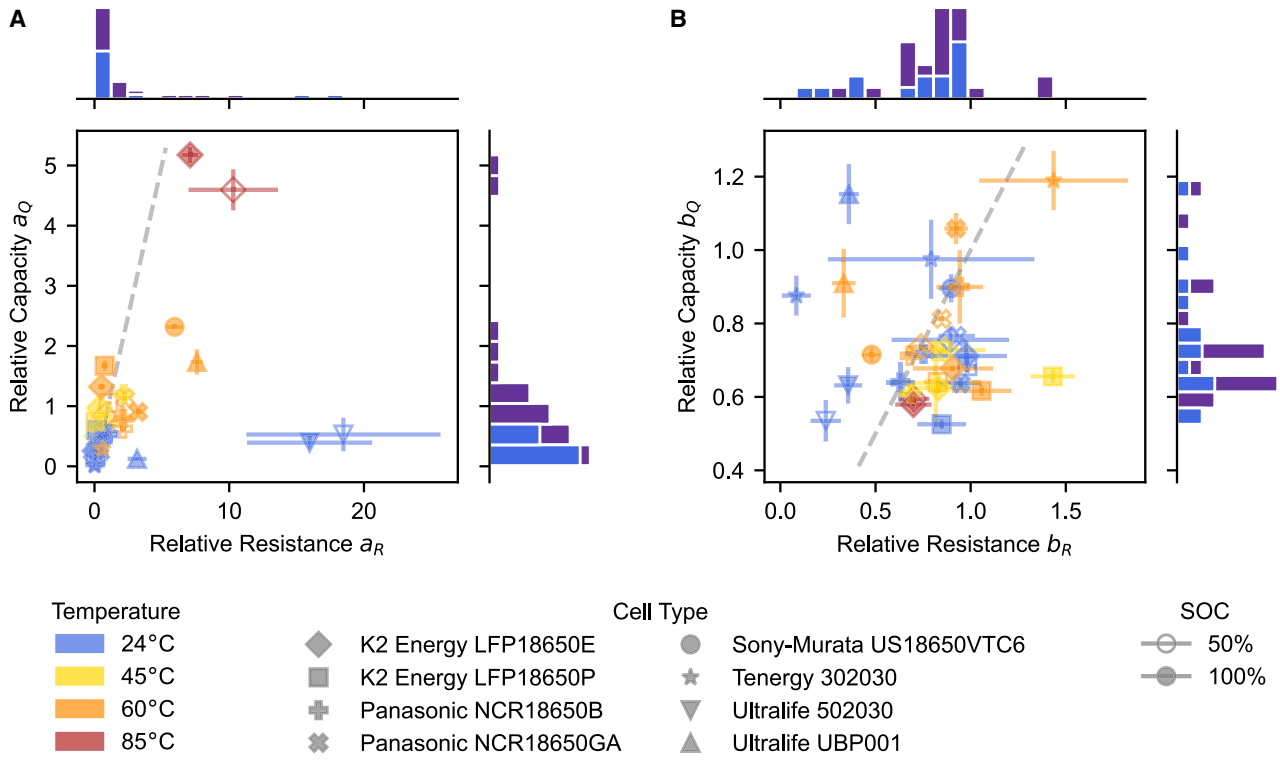

Figure 6. Relative capacity loss vs. relative resistance growth

(A) Scatterplot of the pre-exponential parameters a_Q vs. a_R.

(B) Scatterplot of the exponential parameters b_Q vs. b_R. A gray dotted line is used to show the one-to-one line. The error bar is the standard deviation of repeats. The histograms shown on the sides of the scatterplots are taken from the mean *a* and *b* values for each testing condition and cell type. The contribution of the 24°C data to the histogram is emphasized in blue.

aging.[44,49,50] These models can be extended to be used for calendar aging lifetime predictions. Numerous tools and methods in the literature can address the shortcomings of traditional models regarding the temperature and time dependence of calendar aging, and we encourage the community to utilize the dataset presented in this work to develop accurate and robust models for long-term calendar aging.

Conclusion

In this work, we analyzed eight different cell types with calendar aging data collected over a time frame of up to 13 years, allowing for a systematic analysis that reveals general observations applicable across various cell types. First, we challenge the applicability of the Arrhenius equation under specific assumptions and reveal significant deviations from ideal behavior that result in years of inaccuracy when predicting low-temperature calendar aging. Next, we analyzed the activation energy and showcased that even among seemingly similar cell chemistries from the same manufacturer, the influence of temperature on degradation varies significantly. By analyzing the time dependence of degradation using the power-law exponential (*b*), we demonstrate that the majority of cells regardless of testing conditions deviate significantly from the ideal diffusion-limited $t^{0.5}$ SEI layer growth. This time dependence differs drastically across cell types and between capacity vs. resistance trends. By analyzing the replicates present in this work, we observe substantial cell-to-cell variability in degradation trends under identical storage conditions. Finally, we show that simple power-law extrapolation of room temperature calendar aging data requires nearly 90% of the data prior to the EOL time to accurately predict 90% of cells' EOL within ±0.5 years. Collectively, these observations underscore the challenges in performing accelerated aging studies and highlight the need for long-term ambient temperature calendar aging data to validate calendar aging models. This work advocates for the creation of rigorously developed models that accurately account for these findings to bolster the understanding and prediction of calendar aging degradation. In addition, this work can be further improved by incorporating more finely spaced SOCs, temperatures, and other stress factors to improve the model accuracy to better understand its effect on long-term calendar aging.

METHODS

Experimental setup

The batteries were stored in open circuit conditions in Cincinnati Sub Zero temperature chambers at set points of 24°C, 45°C, 60°C, and 85°C. Cylindrical cells had nickel tabs resistance spot welded on to them. Pouch cells and prismatic cells were already present with tabs. During the diagnostic cycle, the

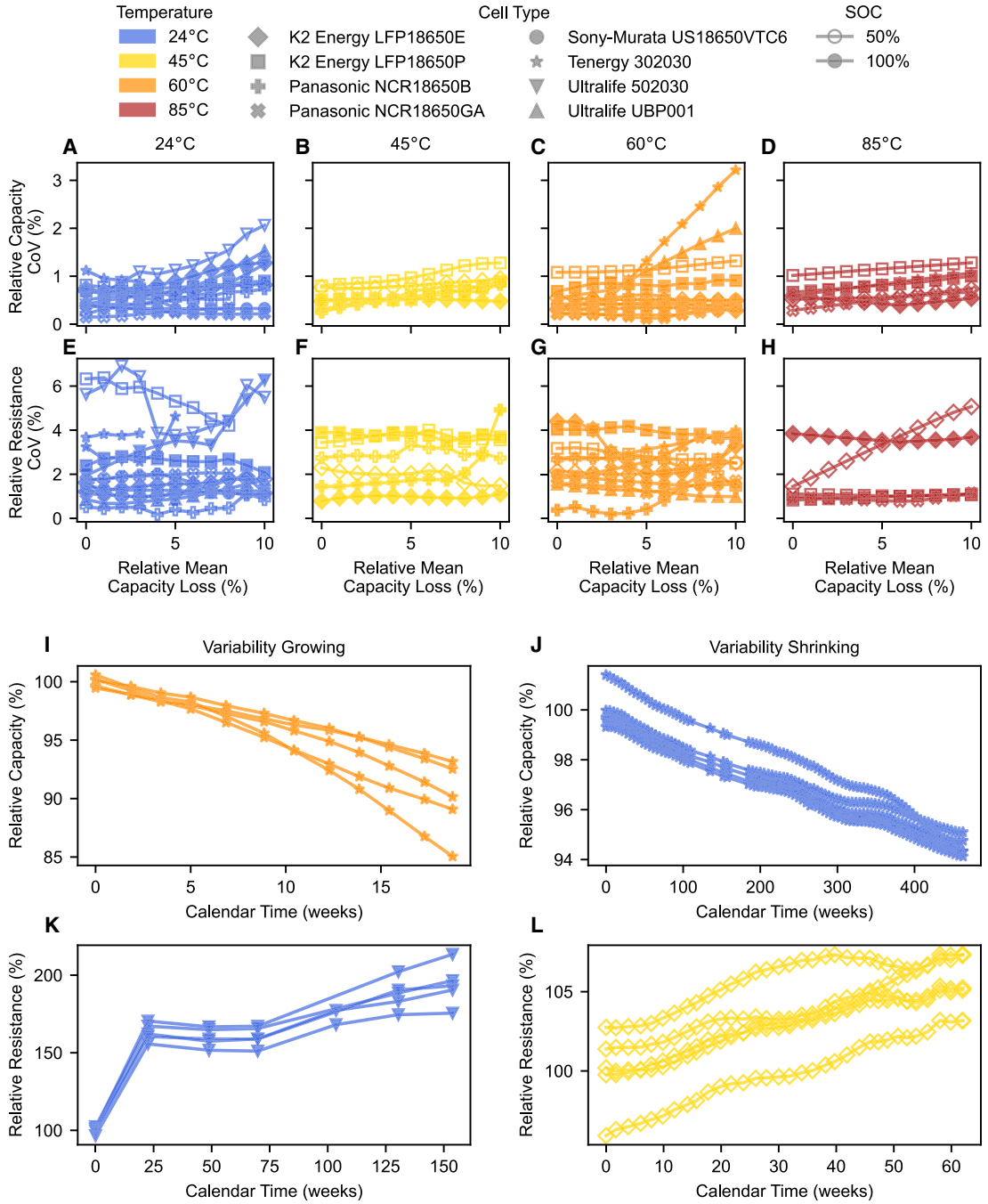

Figure 7. Effect of degradation on cell-to-cell variability

(A–H) For unique cell chemistries and testing conditions, the coefficient of variation (CoV) is calculated for relative capacity and relative resistance as the standard deviation divided by the mean as a function of the relative mean capacity fade. The relative capacities used here are normalized by the mean initial capacity of all repeats instead of their individual initial capacity to represent initial variability properly. The CoV is calculated for every 1% relative mean capacity loss until either 10% fade or data have ended. These data are plotted for capacity at (A) 24°C, (B) 45°C, (C) 60°C, and (D) 85°C. Similarly, for resistance at (E) 24°C, (F) 45°C, (G) 60°C, and (H) 85°C.

(I–L) Examples showing variability growing and shrinking for relative capacity and relative resistance.

batteries were taken out of the chambers and placed in open air of a controlled temperature lab space (24°C ± 4°C). Maccor 4000 potentiostats (calibrated annually) were then connected to the batteries via Mueller BU-75k Kelvin clips with separate voltage sense and current carrying wire to perform the diagnostic cycle (Figure 9A). The diagnostic cycle consists of an initial discharge,

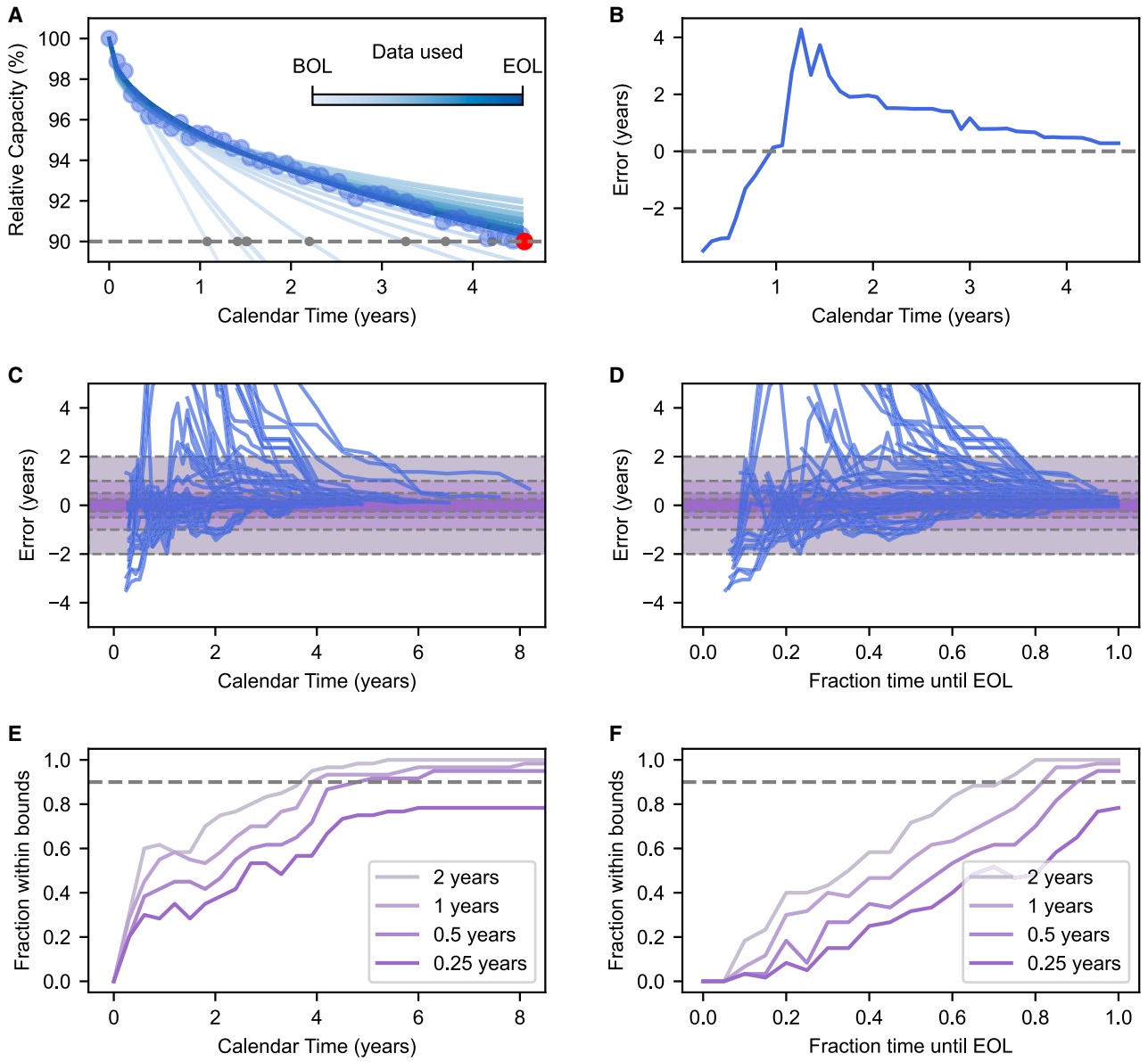

Figure 8. Incremental power-law EOL extrapolation

(A) An example of the methodology of incrementally fitting the power-law on increasing data for a sample cell (C00214, K2 Energy LFP18650E, 24°C, 100% SOC). The data are shown as blue markers, and the incrementally fit power law is shown as solid lines colored from light to dark blue based on how much data from the beginning of life (BOL) to EOL is used. The 90% relative capacity EOL condition is shown as a gray dashed line, and where the fitted power laws cross this condition are shown with gray markers. An additional red dot is included for the true EOL time extracted from the smoothed data.

(B–F) (B) The error trajectory of the fits shown in (A). The error trajectories are then plotted for all 24°C cells against (C) the calendar time in years and (D) the fraction of time until EOL. The y axis is limited to ±5 years to better show error trajectories (for full versions of these plots and separation of cell types see Figure S11). Error boundaries of ±2, 1, 0.5, and 0.25 years are shown in different shades of purple. The fraction of the cells that are within the error boundaries shown in (C) and (D) are shown with their corresponding colors against (E) the calendar time in years, and (F) the fraction of time until EOL. A gray dashed line at 0.9 is included for reference.

three C/5 low-rate cycles, three high-rate cycles, a C/5 capacity check cycle to observe any damage done by high-rate cycles, and a final charge to storage SOC. The 50% storage SOC is a charge from the lower voltage cutoff to 50% of the nominal capacity, and the 100% storage SOC is a charge from the lower cutoff voltage to the upper voltage cutoff. The full details of the diagnostic cycle are described in Table S1. Some of the apparatus and testing conditions used in these experiments can cause slight variations in the capacity and resistance measurements, the effects of which are not further studied in this work. For instance, the tabs may oxidize at higher temperatures and cause an increase in resistance. Minor variations in the force

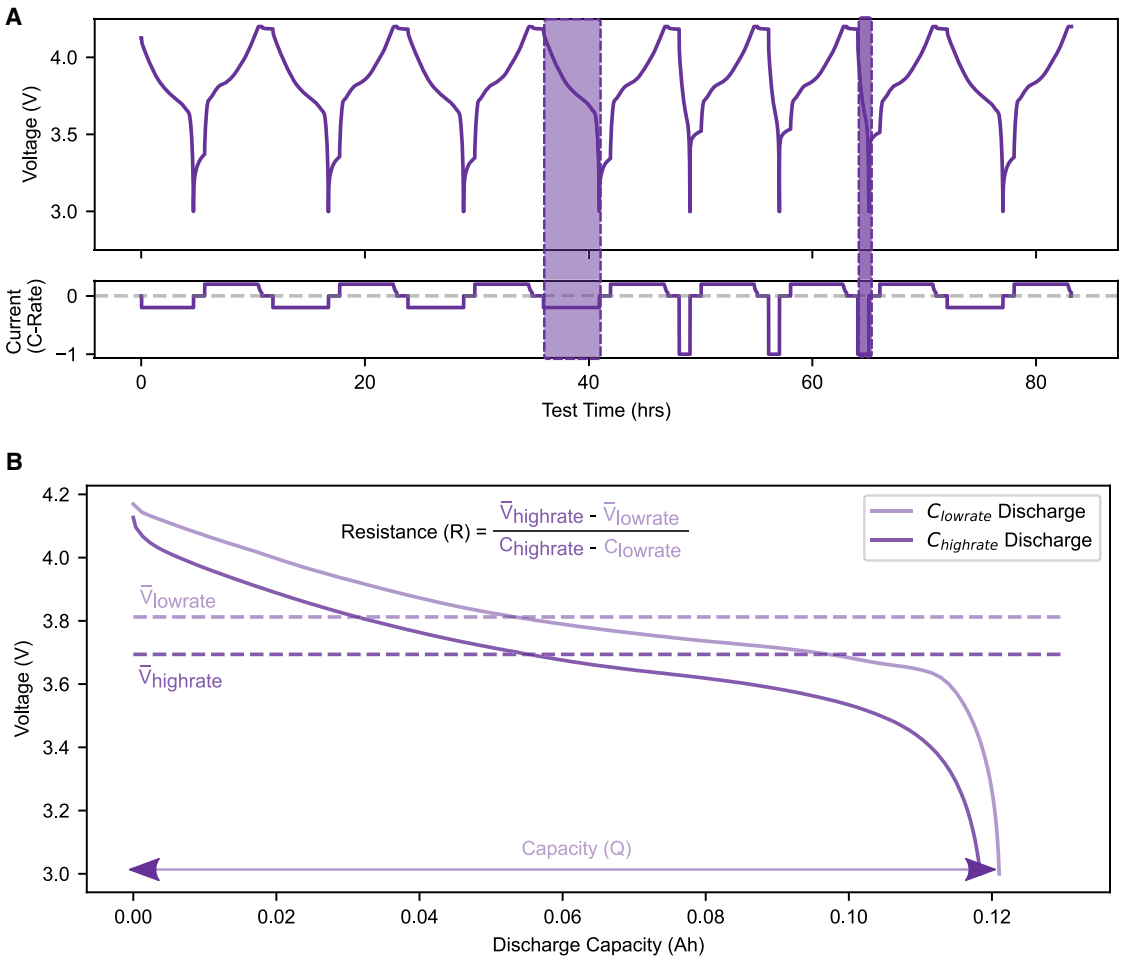

Figure 9. Extracting capacity and resistance

(A) Voltage and current traces for the diagnostic cycle of an example cell (Tenergy 302030 stored at 100% SOC). The diagnostic test consists of three C/5 cycles, three high-rate (1C in this case, see Table S2 for other cell type values) cycles, a C/5 capacity check cycle, and a charge to storage SOC. The highlighted portions represent the discharge curves where the capacity and resistance metrics are extracted from. We chose the third C/5 and high-rate discharge curves.

(B) Traces of the low-rate and high-rate voltage vs. capacity curve. The capacity is extracted from the third low-rate discharge curve. The resistance is extracted from high-rate average voltage ($\bar{V}_{highrate}$) and the C/5 low-rate average voltage ($\bar{V}_{lowrate}$) along with the C rates according to Equation 3. The average voltages are calculated by dividing the discharge energy by the capacity for a given discharge curve.

applied to the cells by the Kelvin clips influence resistance measurements. Additionally, there exists temperature-control-induced performance variations from testing the batteries in an open-air controlled temperature lab space during the diagnostic, as well as non-uniform temperature control within storage temperature chambers.

Capacity and resistance extraction

The capacity and resistance metrics are extracted from the periodic diagnostic test. The capacity used to determine Q_{rel} is extracted from the constant current discharge portion of the third C/5 low-rate cycle (Figure 9). The resistance used in R_{rel} is not a DC pulse resistance. Instead, it is a steady-state resistance taken across the whole operating window using information from both the constant current discharge portion of the third C/5 low-rate ($C_{lowrate}$) cycle and the third high-rate ($C_{highrate}$) cycle. A voltage difference is taken as the difference of the C/5 discharge average voltage ($\bar{V}_{lowrate}$) and the high-rate discharge ($C_{highrate}$) average voltage ($\bar{V}_{highrate}$). This voltage difference is then divided by the difference in C rates to get the resistance metric used (Figure 9B, for $C_{highrate}$, see Table S2).

$$R[\Omega \times Ah] = \frac{\bar{V}_{highrate} - \bar{V}_{lowrate}}{C_{highrate} - C_{lowrate}}. \quad \text{(Equation 3)}$$

This choice of resistance metric measures how much energy is lost by going to higher rates, taking into account average kinetic effects across the whole discharge curve. By using the C rate instead of the absolute current value, this metric is normalized to the capacity of the cell type, allowing different capacity cell types to be properly compared. This metric can also be seen as an electrode area normalized resistance under the

assumption that nominal capacity ($Q_{nominal}$) is proportional to the active area that current passes through on the electrode material (see Equation S9).

Data smoothing

The resistance and capacity data contain measurement noise that can obscure the general trend in the data (Figures S12–S15). To counteract this issue, when the data are plotted directly, local polynomial regression with a nominal window size of 14 data points is used to smooth the data points. This type of smoothing performs poorly at the edges of the data; therefore, to better capture the trends at the beginning of testing and EOT, the window size is continuously decreased to half the nominal window size (seven data points). The initial smoothed data point is set to be the same as the raw data for easy comparison. If the total number of data points is less than or equal to 10, smoothing is not applied, and the data are used directly. The smoothed data are used when the data are plotted directly, such as in Figures 1, 2A, and 7, as well as for determining the EOL time. The unsmoothed data, however, is used in fitting the power laws to not introduce any biases induced by the smoothing.

Power-law fitting

The power-law equations (Equations 1 and 2) are fit on the non-smoothed data capacity and time data. The time is input in weeks, and the capacity is input as the relative capacity (%). The data points used are specifically taken from values up until the EOL time. The EOL time is determined from the smoothed data, and if there are not enough total data points ($\geq$ 3) to perform the smoothing procedure, the fitting is not performed. If there is less than three data points after dropping all data past the EOL time, the fit is not performed leading to the exclusion of several 85°C data. If a cell has not reached EOL, all available data points were used until current EOT. To see the data that the power-law equations were fit on, see Figures S16–S19).

A SciPy differential evolution algorithm with a mean absolute error objective function was used to fit the *a* and *b* coefficients. The possible values of the prefactor *a* are constrained between 0 and 1,000, whereas the possible values of *b* are constrained between 0 and 10. The fit values are constrained to be positive, but the upper bounds are chosen to be large enough to allow effectively unconstrained fittings.

Power-law prediction

To understand the influence of increasing the amount of data on the prediction of EOL time, we employ an incremental fitting approach on the data using a power law. We begin fitting the power law with at least four data points, and we incrementally add the following data one at a time until the final data point before the EOL time. At each time point, we calculate the predicted EOL time from the power-law fit and compare it with the true EOL time obtained from the smoothed version of the capacity data (Figures 8A and 8B). To obtain Figures 8E and 8F, the error trajectory is linearly interpolated vs. calendar time or fraction time until EOL, respectively. Beyond the EOL time of a battery, the predicted EOL continues to be the value using the data up until the last data point before the EOL time.

RESOURCE AVAILABILITY

Lead contact

Inquiries regarding the data associated with this paper should be directed to the lead contact, Will Chueh (wchueh@stanford.edu).

Materials availability

This study did not generate new materials.

Data and code availability

Calendar aging data and code including raw data, processed data, fitting results, and figure generating code are included at the following Open Science Framework repository: https://osf.io/ju325/.

ACKNOWLEDGMENTS

This effort was sponsored in whole or in part by the United States Government (USG). The U.S. Government is authorized to reproduce and distribute original submissions for publication for Governmental purposes notwithstanding any copyright notation thereon. The views and conclusions contained herein are those of the authors and should not be interpreted as necessarily representing the official policies or endorsements, either expressed or implied, of the United States Government (USG).

AUTHOR CONTRIBUTIONS

V.N.L., X.C., and F.S., contributed to data analysis, cleaning, and management. V.N.L. generated the figures. V.N.L. and M.U. wrote and revised the manuscript. S.O. and W.C.C. supervised the work and acquired funding for the project. All authors contributed to editing the manuscript.

DECLARATION OF INTERESTS

X.C. is with the Department of Electrical and Computer Engineering, University of California, Los Angeles, California, USA. F.S. is with the Institute for Sustainable Energy systems, University of Applied Science HM, Munich, Germany. They were both affiliated with Stanford University at the time the research was conducted.

SUPPLEMENTAL INFORMATION

Supplemental information can be found online at https://doi.org/10.1016/j.joule.2024.11.013.

Received: July 3, 2024
Revised: October 22, 2024
Accepted: November 22, 2024
Published: December 18, 2024

REFERENCES

1. Jaiswal, A. (2017). Lithium-ion battery based renewable energy solution for off-grid electricity: A techno-economic analysis. Renew. Sustain. Energy Rev. *72*, 922–934. https://doi.org/10.1016/j.rser.2017.01.049.
2. Stampatori, D., Raimondi, P.P., and Noussan, M. (2020). Li-ion batteries: a review of a key technology for transport decarbonization. Energies *13*, 2638. https://doi.org/10.3390/en13102638.
3. Chen, T., Jin, Y., Lv, H., Yang, A., Liu, M., Chen, B., Xie, Y., and Chen, Q. (2020). Applications of lithium-ion batteries in grid-scale energy storage systems. Trans. Tianjin Univ. *26*, 208–217. https://doi.org/10.1007/s12209-020-00236-w.
4. Kucevic, D., Tepe, B., Englberger, S., Parlikar, A., Mühlbauer, M., Bohlen, O., Jossen, A., and Hesse, H. (2020). Standard battery energy storage

system profiles: analysis of various applications for stationary energy storage systems using a holistic simulation framework. J. Energy Storage *28*, 101077. https://doi.org/10.1016/j.est.2019.101077.

5. Christophersen, J.P. (2015). Battery test manual for electric vehicles, revision 3. Idaho National Lab. https://doi.org/10.2172/1186745.
6. Moody, J., Farr, E., Papagelis, M., and Keith, D.R. (2021). The value of car ownership and use in the United States. Nature Sustainability *4*, 769–774. https://doi.org/10.1038/s41893-021-00731-5.
7. Keil, P., Schuster, S.F., Wilhelm, J., Travi, J., Hauser, A., Karl, R.C., and Jossen, A. (2016). Calendar aging of lithium-ion batteries. J. Electrochem. Soc. *163*, A1872–A1880. https://doi.org/10.1149/2.0411609jes.
8. Dufek, E.J., Tanim, T.R., Chen, B.R., and Sangwook, K. (2022). Battery calendar aging and machine learning. Joule *6*, 1363–1367. https://doi.org/10.1016/j.joule.2022.06.007.
9. Geisbauer, C., Wöhrl, K., Koch, D., Wilhelm, G., Schneider, G., and Schweiger, H.G. (2021). Comparative study on the calendar aging behavior of six different lithium-ion cell chemistries in terms of parameter variation. Energies *14*, 3358. https://doi.org/10.3390/en14113358.
10. Liu, K., Li, Y., Hu, X., Lucu, M., and Widanage, W.D. (2020). Gaussian process regression with automatic relevance determination kernel for calendar aging prediction of lithium-ion batteries. IEEE Trans. Ind. Inf. *16*, 3767–3777. https://doi.org/10.1109/tii.2019.2941747.
11. Azkue, M., Lucu, M., Martinez-Laserna, E., and Aizpuru, I. (2021). Calendar ageing model for li-ion batteries using transfer learning methods. World Electr. Veh. J. *12*, 145. https://doi.org/10.3390/wevj12030145.
12. Ramadass, P., Haran, B., Gomadam, P.M., White, R., and Popov, B.N. (2004). Development of first principles capacity fade model for li-ion cells. J. Electrochem. Soc. *151*, A196. https://doi.org/10.1149/1.1634273.
13. Safari, M., Morcrette, M., Teyssot, A., and Delacourt, C. (2009). Multimodal physics-based aging model for life prediction of li-ion batteries. J. Electrochem. Soc. *156*, A145. https://doi.org/10.1149/1.3043429.
14. Storch, M., Hahn, S.L., Stadler, J., Swaminathan, R., Vrankovic, D., Krupp, C., and Riedel, R. (2019). Post-mortem analysis of calendar aged large-format lithium-ion cells: investigation of the solid electrolyte interphase. J. Power Sources *443*, 227243. https://doi.org/10.1016/j.jpowsour.2019.227243.
15. Zhu, W., Zhou, P., Ren, D., Yang, M., Rui, X., Jin, C., Shen, T., Han, X., Zheng, Y., Lu, L., et al. (2022). A mechanistic calendar aging model of lithium-ion battery considering solid electrolyte interface growth. Int. J. Energy Res. *46*, 15521–15534. https://doi.org/10.1002/er.8249.
16. Ploehn, H.J., Ramadass, P., and White, R.E. (2004). Solvent diffusion model for aging of lithium-ion battery cells. J. Electrochem. Soc. *151*, A456. https://doi.org/10.1149/1.1644601.
17. Broussely, M., Herreyre, S., Biensan, P., Kasztejna, P., Nechev, K., and Staniewicz, R.J. (2001). Aging mechanism in li ion cells and calendar life predictions. J. Power Sources *97*, 13–21. https://doi.org/10.1016/S0378-7753(01)00722-4.
18. Schimpe, M., von Kuepach, M.E., Naumann, M., Hesse, H.C., Smith, K., and Jossen, A. (2018). Comprehensive modeling of temperature-dependent degradation mechanisms in lithium iron phosphate batteries. J. Electrochem. Soc. *165*, A181–A193. https://doi.org/10.1149/2.1181714jes.
19. Ecker, M., Nieto, N., Käbitz, S., Schmalstieg, J., Blanke, H., Warnecke, A., and Sauer, D.U. (2014). Calendar and cycle life study of li(nimnco)o2-based 18650 lithium-ion batteries. J. Power Sources *248*, 839–851. https://doi.org/10.1016/j.jpowsour.2013.09.143.
20. Bischof, K., Flügel, M., Hölzle, M., Wohlfahrt-Mehrens, M., and Waldmann, T. (2024). Aging mechanism for calendar aging of li-ion cells with si/graphite anodes. J. Electrochem. Soc. *171*, 10510. https://doi.org/10.1149/1945-7111/ad1b7c.
21. Sarasketa-Zabala, E., Gandiaga, I., Rodriguez-Martinez, L.M., and Villarreal, I. (2014). Calendar ageing analysis of a lifepo4/graphite cell with dynamic model validations: towards realistic lifetime predictions. J. Power Sources *272*, 45–57. https://doi.org/10.1016/j.jpowsour.2014.08.051.
22. Naumann, M., Schimpe, M., Keil, P., Hesse, H.C., and Jossen, A. (2018). Analysis and modeling of calendar aging of a commercial lifepo4/graphite cell. J. Energy Storage *17*, 153–169. https://doi.org/10.1016/j.est.2018.01.019.
23. Hayder, A., Beltran, H., Lindsey, N.J., and Pecht, M. (2023). Assessment of the calendar aging of lithium-ion batteries for a long-term—space missions. Front. Energy Res. *11*. https://doi.org/10.3389/fenrg.2023.1108269.
24. Attia, P.M., Chueh, W.C., and Harris, S.J. (2020). Revisiting the t0.5 dependence of SEI growth. J. Electrochem. Soc. *167*, 090535. https://doi.org/10.1149/1945-7111/ab8ce4.
25. Hahn, S.L., Storch, M., Swaminathan, R., Obry, B., Bandlow, J., and Birke, K.P. (2018). Quantitative validation of calendar aging models for lithium-ion batteries. J. Power Sources *400*, 402–414. https://doi.org/10.1016/j.jpowsour.2018.08.019.
26. Karger, A., Schmitt, J., Kirst, C., Singer, J.P., Wildfeuer, L., and Jossen, A. (2023). Mechanistic calendar aging model for lithium-ion batteries. J. Power Sources *578*, 233208. https://doi.org/10.1016/j.jpowsour.2023.233208.
27. Broussely, M., Biensan, P., Bonhomme, F., Blanchard, P., Herreyre, S., Nechev, K., and Staniewicz, R.J. (2005). Main aging mechanisms in li ion batteries. Journal of Power Sources *146*, 90–96. https://doi.org/10.1016/j.jpowsour.2005.03.172.
28. Hendricks, C.E., Mansour, A.N., Fuentevilla, D.A., Waller, G.H., Ko, J.K., and Pecht, M.G. (2020). Copper dissolution in overdischarged lithium-ion cells: X-ray photoelectron spectroscopy and x-ray absorption fine structure analysis. J. Electrochem. Soc. *167*, 90501. https://doi.org/10.1149/1945-7111/ab697a.
29. Lee, Y.K. (2021). Effect of transition metal ions on solid electrolyte interphase layer on the graphite electrode in lithium ion battery. J. Power Sources *484*, 229270. https://doi.org/10.1016/j.jpowsour.2020.229270.
30. Joshi, T., Eom, K., Yushin, G., and Fuller, T.F. (2014). Effects of dissolved transition metals on the electrochemical performance and sei growth in lithium-ion batteries. J. Electrochem. Soc. *161*, A1915–A1921. https://doi.org/10.1149/2.0861412jes.
31. Schmalstieg, J., Käbitz, S., Ecker, M., and Sauer, D.U. (2014). A holistic aging model for li(nimnco)o2 based 18650 lithium-ion batteries. J. Power Sources *257*, 325–334. https://doi.org/10.1016/j.jpowsour.2014.02.012.
32. Gewald, T., Lienkamp, M., Lehmkuhl, D., and Hahn, A. (2019). Accelerated aging characterization of lithium-ion cells: Limitation of arrhenius dependency. IEEE, 1–10. https://doi.org/10.1109/EVER.2019.8813534.
33. Gasper, P., Saxon, A., Shi, Y., Endler, E., Smith, K., and Thakkar, F.M. (2023). Degradation and modeling of large-format commercial lithium-ion cells as a function of chemistry, design, and aging conditions. J. Energy Storage *73*, 109042. https://doi.org/10.1016/j.est.2023.109042.
34. Gasper, P., Gering, K., Dufek, E., and Smith, K. (2021). Challenging practices of algebraic battery life models through statistical validation and model identification via machine-learning. J. Electrochem. Soc. *168*, 20502. https://doi.org/10.1149/1945-7111/abdde1.
35. Gauthier, R., Luscombe, A., Bond, T., Bauer, M., Johnson, M., Harlow, J., Louli, A., and Dahn, J.R. (2022). How do depth of discharge, c-rate and calendar age affect capacity retention, impedance growth, the electrodes, and the electrolyte in li-ion cells? J. Electrochem. Soc. *169*, 20518. https://doi.org/10.1149/1945-7111/ac4b82.
36. Eddahech, A., Briat, O., and Vinassa, J.-M. (2015). Performance comparison of four lithium–ion battery technologies under calendar aging. Energy *84*, 542–550. https://doi.org/10.1016/j.energy.2015.03.
37. Dubarry, M., and Devie, A. (2018). Battery durability and reliability under electric utility grid operations: representative usage aging and calendar aging. J. Energy Storage *18*, 185–195. https://doi.org/10.1016/j.est.2018.04.004.
38. Krupp, A., Beckmann, R., Diekmann, T., Ferg, E., Schuldt, F., and Agert, C. (2022). Calendar aging model for lithium-ion batteries considering the

influence of cell characterization. J. Energy Storage *45*, 103506. https://doi.org/10.1016/j.est.2021.103506.

39. Frie, F., Ditler, H., Klick, S., Stahl, G., Rahe, C., Ghaddar, T., and Sauer, D.U. (2024). An analysis of calendaric aging over 5 years of Ni-rich 18650-cells with Si/C anodes. ChemElectroChem *202400020*. ChemElectroChem *11*, e202400020. https://doi.org/10.1002/celc.202400020.

40. Lucu, M., Martinez-Laserna, E., Gandiaga, I., Liu, K., Camblong, H., Widanage, W.D., and Marco, J. (2020). Data-driven nonparametric Li-ion battery ageing model aiming at learning from real operation data – part A: storage operation. J. Energy Storage *30*, 101409. https://doi.org/10.1016/j.est.2020.101409.

41. Lewerenz, M., Käbitz, S., Knips, M., Münnix, J., Schmalstieg, J., Warnecke, A., and Sauer, D.U. (2017). New method evaluating currents keeping the voltage constant for fast and highly resolved measurement of arrhenius relation and capacity fade. J. Power Sources *353*, 144–151. https://doi.org/10.1016/j.jpowsour.2017.03.136.

42. Ecker, M., Gerschler, J.B., Vogel, J., Käbitz, S., Hust, F., Dechent, P., and Sauer, D.U. (2012). Development of a lifetime prediction model for lithium-ion batteries based on extended accelerated aging test data. J. Power Sources *215*, 248–257. https://doi.org/10.1016/j.jpowsour.2012.05.012.

43. Waldmann, T., Wilka, M., Kasper, M., Fleischhammer, M., and Wohlfahrt-Mehrens, M. (2014). Temperature dependent ageing mechanisms in lithium-ion batteries - a post-mortem study. J. Power Sources *262*, 129–135. https://doi.org/10.1016/j.jpowsour.2014.03.112.

44. Alghalayini, M., Harris, S.J., Harris, S., and Noack, M.M. (2024). Early prediction of the failure probability distribution for energy storage technologies driven by domain-knowledge-informed machine learning. https://doi.org/10.21203/rs.3.rs-3871499/v1.

45. Christophersen, J.P. (2012). Battery technology life verification test manual revision 1. https://doi.org/10.2172/1064046.

46. Kamyab, N., Weidner, J.W., and White, R.E. (2019). Mixed mode growth model for the solid electrolyte interface (SEI). J. Electrochem. Soc. *166*, A334–A341. https://doi.org/10.1149/2.1101902jes.

47. Khaleghi Rahimian, S., Forouzan, M.M., Han, S., and Tang, Y. (2020). A generalized physics-based calendar life model for Li-ion cells. Electrochim. Acta *348*. https://doi.org/10.1016/j.electacta.2020.136343.

48. Gasper, P., Collath, N., Hesse, H.C., Jossen, A., and Smith, K. (2022). Machine-learning assisted identification of accurate battery lifetime models with uncertainty. J. Electrochem. Soc. *169*, 80518. https://doi.org/10.1149/1945-7111/ac86a8.

49. Chu, A., Allam, A., Cordoba Arenas, A., Rizzoni, G., and Onori, S. (2020). Stochastic capacity loss and remaining useful life models for lithium-ion batteries in plug-in hybrid electric vehicles. J. Power Sources *478*, 228991. https://doi.org/10.1016/j.jpowsour.2020.228991.

50. Barbers, E., Hust, F.E., Hildenbrand, F.E.A., Frie, F., Quade, K.L., Bihn, S., Sauer, D.U., and Dechent, P. (2024). Exploring the effects of cell-to-cell variability on battery aging through stochastic simulation techniques. J. Energy Storage *84*, 110851. https://doi.org/10.1016/j.est.2024.110851.